Title
Formation of Strong Brønsted Acid Sites on Aluminosilicate Surfaces during Catalytic Cracking

Journal
ACS Catalysis

Authors
Sawant, Kaustubh J
Stockwell, David
Debellis, Anthony
et al.

Publication Date
2026-09-10

DOI
10.1021/acscatal.6c03544

Formation of Strong Brønsted Acid Sites on Aluminosilicate Surfaces during Catalytic Cracking

*Kaustubh J. Sawant[1], David Stockwell[2], Anthony Debellis[2], Roel Sanchez-Carrera[3], Lucas Dorazio[2], Philippe Sautet[1,4]**

[1]Chemical and Biomolecular Engineering Department, University of California, Los Angeles, Los Angeles, CA 90095

[2]BASF Corporation, 100 Park Avenue, Florham Park, NJ 07932

[3]BASF Corporation, 327B Hildebrand Hall, University of California, Berkeley, Berkeley, CA 94720

[4]Chemistry and Biochemistry Department, University of California, Los Angeles, Los Angeles, CA 90095

Keywords: Amorphous Aluminosilicates, Catalytic Cracking, Brønsted Acidity, Mullite, Si-doped γ-Al_2O_3

Abstract:

Amorphous aluminosilicates are essential components of fluid catalytic cracking (FCC) catalysts, where they provide structural support, hierarchical porosity, and acid functionality within the mesoporous matrix. A molecular-level description of the active acid site ensemble remains challenging because these materials are compositionally heterogeneous and structurally disordered. Most experimental and theoretical studies have focused on Si-doped γ-Al_2O_3 that serves as a convenient model system. Here, we move beyond this simplified representation toward more realistic and chemically complex aluminosilicate structures. We combine density functional theory (DFT), equivariant machine-learning interatomic potentials (MLIPs), and grand-canonical basin hopping (GCBH) to map structure-acidity relationships for aluminosilicate compositions that arise under FCC-relevant hydrothermal conditions (T=550°C and P_{H_2O}=1.2 bar), representative of the reactor inlet. We study a family of mullite surfaces across Al_2O_3:SiO_2 ratios (denoted *n:m*) and associated oxygen-vacancy contents, and we explicitly model additional SiO_2 deposition to emulate silica redistribution during phase evolution from kaolin through spinel intermediates to mullite. Machine-learning potentials trained on structurally related sillimanite surfaces accurately describe Al-Si-O-H chemistry and transfer to vacancy-rich and silica-modified mullite phases. Using NH_3 binding as a descriptor of Brønsted acidity, we find that mullite can host acid sites with strengths reaching ΔE_{NH_3} ≈ -140 kJ mol^{-1} in 3:2 mullite, which is comparable to external zeolitic acid sites and substantially stronger than those reported on Si-doped γ-Al_2O_3. Silica grafting onto otherwise weakly acidic mullite terminations further generates an ensemble of strong bridging and pseudo-bridging Brønsted acid sites. We attribute this enhanced acidity to the local emergence of tetrahedrally coordinated Al^{IV} environments that strongly polarize Al-OH-Si linkages. These

results identify defect-rich as well as silica-decorated mullite surfaces as a realistic and potentially dominant source of strong matrix acidity in FCC catalysts under operating conditions.

Introduction

Catalytic cracking relies on solid acids[1], with overall performance determined by the density, strength, and accessibility of active sites within a porous composite catalyst[2]. The primary active components are zeolite nanoparticles which possess strong, well-defined Brønsted acid sites, making them highly effective catalysts for hydrocarbon cracking[3,4]. However, their intrinsic microporosity restricts access to bulky feed molecules[5], which are relevant for biofuels and heavy fractions (bottoms cracking). Industrial FCC catalysts therefore contain a matrix/binder/filler network in addition to the zeolite phase. Depending on the formulation, this matrix may include kaolin-derived clay phases, alumina or boehmite-derived binders, silica, silica–alumina, and other stabilizing or contaminant-trapping components.[6,7]. In some cases, this matrix is formed directly from kaolin-derived phases [8,9]. In addition to providing mechanical integrity, the amorphous aluminosilicate contributes additional Brønsted and Lewis acid sites, weaker than those in zeolites[10,11] but more accessible via meso- and macro-porosity that enhances diffusion of reactants and products[4].

The calcination of kaolin derived matrix proceeds through metakaolin and spinel intermediates, culminating in the formation of mullite[12]. Mullite is a family of vacancy-containing aluminosilicates, described as $Al_{4+2x}Si_{2-2x}O_{10-x}$, where x equals the oxygen-vacancy content[13]. Within this compositional framework, an increase of x by one is equivalent to removing two SiO_2 units and adding one Al_2O_3 unit, thereby maintaining charge neutrality and the nominal oxidation states of all elements. The composition is commonly reported as an Al_2O_3:SiO_2 ratio (denoted n:m). This thermally robust aluminosilicate is an important component of the catalyst, to which it imparts critical meso and macro-porosity and structural stability[14]. Despite its fundamental role, a significant knowledge gap persists regarding the intrinsic surface acidic properties of mullites and

their subsequent impact on the catalytic cracking performance of the composite material[15]. Current understanding of acidity in these systems is largely inferred from studies on model phases, particularly Si-doped γ-alumina[16–22], which represents the spinel intermediate. Here, "spinel" follows the terminology commonly used in the FCC industrial community for the kaolin-derived alumina-rich intermediate and does not necessarily denote a crystallographically well-defined spinel phase. These model systems have provided important insight into Brønsted acid-site formation, but they do not directly resolve the acid-site diversity, strength, and distribution within mullite phases. To address this gap, we systematically investigate a series of mullite phases spanning experimentally relevant compositions as well as vacancy-rich, silica-poor limits. For each stoichiometry, we construct stable low-index surface terminations and then study the hydroxylation and reconstruction of the surface under FCC-relevant steam chemical potentials using grand-canonical basin hopping.

Realistic atomistic modeling of mullite-family aluminosilicates is challenging because mullite is not a single fixed compound but a defect-tolerant aluminosilicate solid solution in which variations in Al/Si ratio are accommodated by crystallographically intrinsic oxygen vacancies while maintaining overall charge neutrality[23–25]. The most abundant compositions are 2:1 mullite (x = 0.4 | $Al_{4.8}Si_{1.2}O_{9.6}$ | $2Al_2O_3$:$1SiO_2$) and 3:2 mullite (x = 0.25 | $Al_{4.5}Si_{1.5}O_{9.75}$ | $3Al_2O_3$:$2SiO_2$)[26], which contain 312 and 252 atoms per primitive cell, respectively. Systematically enumerating different surface terminations, hydroxylation coverage, and probe-molecule adsorption across chemical-potential ranges, which are relevant to our study, with expensive Density Functional Theory (DFT) calculations is highly challenging and cost-prohibitive. To make this exploration tractable, we adopt a transfer-learning strategy that begins with the simpler mineral sillimanite (x = 0 | Al_2SiO_5; $1Al_2O_3$:$1SiO_2$), which is chemically and structurally closely related to mullite and can

be viewed as the 1:1 ("sillimanite-limit") end member of the broader mullite-family. The key difference is the presence of oxygen vacancies in mullite with a vacancy concentration in the range (x) ≈ 0.20 - 0.57. Utilizing this structural and chemical similarity, we develop a machine-learning interatomic potential (MLIP)[27] for the Al-Si-O-H chemical space that is trained on DFT data for pristine and hydroxylated sillimanite surfaces. This MLIP is validated on mullite structures, enabling rapid and accurate exploration. We use a grand canonical basin hopping [28,29] approach to sample configurations under conditions relevant to the FCC reaction. Specifically, we consider representative industrial operating conditions of T= 550°C and P_{H_2O}= 1.2 bar ($\Delta\mu_{H_2O}$= -1.05eV), which approximate the environment at the FCC reactor inlet, where 2 wt% H_2O is mixed with 98 wt% gas oil at zero conversion. This hybrid DFT/MLIP workflow [22] allows us to identify low-energy mullite surface terminations and hydroxyl coverages, map the distribution and relative abundance of acid-site motifs, and evaluate key acidity descriptors such as NH_3 binding energies. To explicitly model ammonia adsorption, we generated an additional DFT dataset by adsorbing NH_3 on a randomly selected set of hydroxylated sillimanite structures. The resulting MLIP was then applied to optimize NH_3 adsorbed mullite surfaces.

Our calculations indicate that mullite can host strong Brønsted acid sites under hydrothermal FCC conditions. Although mullite terminations are dominated by aluminol and silanol groups that are only weakly acidic, we identify a distinct class of zeolite-like Al-OH-Si bridging motifs that emerge on certain mullite surfaces. These sites are rare, with an areal density of only about 0.3-0.6 nm^{-2}. Note that all reported hydroxyl, acid-site, and silica coverages are normalized by the exposed area of the modeled surface/facet. In particular, the most stable 3:2 mullite phase can form bridging Brønsted acid sites with acid strength exceeding that typically reported for the widely used Si-doped γ-Al_2O_3 model.

To connect these motifs to catalyst evolution, we begin with the kaolin-to-mullite transformation pathway, which proceeds through a biphasic γ-Al_2O_3/SiO_2 (spinel) intermediate and is accompanied by redistribution of excess silica as mullite forms[30]. We hypothesize that excess silica, whether released during phase evolution or retained from the crystallization mother liquor in industrial synthesis process[6], can graft onto defect-rich mullite surfaces and generate local environments that favor the formation of strong Brønsted acid sites. To test this idea, we explicitly modeled silica deposition on representative mullite surface terminations spanning both silica-rich and vacancy-rich regimes. On the relatively weakly acidic 3.5:2 mullite surface, we find that silica grafting produces a coverage-dependent enhancement in Brønsted acidity, with an optimum silica loading that gives rise to highly acidic zeolite-like bridging and pseudo-bridging motifs. In contrast, on the more defect-rich 5:2 mullite surface, additional silica can quench the most reactive local environments and partially passivate strong Brønsted acid sites.

These findings expand the mechanistic and structural picture of FCC matrix acidity beyond Si-doped alumina, the phase most commonly used as the model system in both experimental and computational studies, and indicate that mullite-based aluminosilicate motifs can also contribute to Brønsted acidity under realistic FCC reactor inlet conditions.

Results and discussion

Mullite Surface under Reaction Conditions

We investigated multiple mullite stoichiometries spanning a broad range of crystallographically defined oxygen-vacancy concentrations. For each composition, surface slabs were generated from a single bulk parent structure taken from the DFT-derived and experimentally validated models of Klar et al. [25] We selected the lowest-energy DFT-optimized bulk structure for each composition and did not explicitly consider metastable bulk orderings. This choice was made to provide one

crystallographically consistent and physically motivated reference structure per stoichiometry, rather than introducing additional variability from multiple possible bulk orderings, which would be computationally intractable and beyond the scope of the present work. While mullite is a modulated aluminosilicate with coupled Al/Si and oxygen-vacancy ordering, the selected Klar et al. structures capture the essential composition dependent bulk ordering and provide a starting point for comparative surface studies. Previous studies [25] have shown that mullite becomes progressively less thermodynamically stable as the vacancy content increases (i.e., as the bulk silica concentration decreases), and that the bulk energetics correlate approximately linearly with vacancy concentration (Figure 1a). To establish a baseline picture of intrinsic surface stability, we first evaluated pristine slabs. We considered both non-polar terminations and type-II polar terminations (different atomic layer compositions on the two sides of the slab) for the low-Miller-index (001), (010), (011), (100), (101), and (111) facets across four mullite stoichiometries (3:2, 3.5:2, 2:1, and 5:2), along with sillimanite (1:1). The identity of the most stable termination depends on stoichiometry; a complete ranking is provided in Figure S3a. In general, pristine surface energies follow the same qualitative stability trend as the bulk, but the dependence on composition is not strictly linear. Specific termination combinations are relatively stabilized or destabilized compared with expectations from bulk energetics alone.

To distinguish termination stability from facet abundance, we constructed Wulff morphologies using the lowest-energy pristine termination for each facet from Figure S3. The resulting area fractions, summarized in Table S4, show a strong dependence on composition. Sillimanite is dominated by the (100), (111), and (011) facets, 3:2 mullite by the (101) facet, and 3.5:2 and 2:1 mullite by significant (110) contributions. In contrast, 5:2 mullite shows a more distributed morphology across the (101), (100), (010), and (011) facets.

These Wulff constructions provide a pristine, dry-surface thermodynamic reference. Hydration, hydroxylation, or reconstruction under hydrothermal or pretreatment conditions may alter the relative surface energies and equilibrium morphology. A complete hydrated/reconstructed Wulff analysis is beyond the scope of this work, although comparison of hydrated 3.5:2 mullite (100) and (010) facets did not show an inversion in relative stability. Although these pristine Wulff constructions cannot be used to rigorously determine crystallite-averaged acid-site densities under hydrothermal conditions, they provide useful context for assessing the potential relevance of the reactive surfaces identified below. For 3:2 mullite, the (101) facet accounts for approximately 46.6% of the calculated Wulff surface area and is also the surface on which we identify a strongly acidic Al-O(H)-Si Brønsted acid site. Thus, for this composition, strong intrinsic acidity coincides with a thermodynamically abundant facet. In contrast, the (001) facet of 5:2 mullite hosts the strongest Brønsted acid site identified in this work but accounts for only approximately 1.0% of the calculated pristine Wulff area. This comparison highlights the distinction between site strength and site abundance: the experimentally relevant contribution of a surface motif depends on both its intrinsic acidity and the abundance of the facet and termination on which it occurs.

Because realistic surfaces are expected to reconstruct and hydroxylate under reaction conditions, an exhaustive treatment of all terminations is beyond our current computational scope. We therefore focused the analysis on the lowest-energy pristine termination for each facet and stoichiometry. This selection identifies the most stable termination within a given facet family, but it does not necessarily correspond to the facet with the largest exposed area in the equilibrium particle morphology. For polar slabs, the two exposed bottom and top surfaces are chemically distinct; accordingly, the top and bottom surfaces were hydroxylated independently in the grand-canonical basin hopping (GCBH) sampling. GCBH under FCC-relevant conditions shows that

hydroxylation substantially lowers the absolute surface energies while preserving the relative facet stability ordering (Figure 1b). Analysis of the corresponding Boltzmann populations at 550 °C shows that sillimanite is strongly dominated by a single hydroxylated motif. The mullite compositions exhibit broader low-energy ensembles with several structures contributing to the equilibrium population (Figure 1e). This indicates that some mullite surfaces are thermodynamically more fluxional under reaction conditions. Because the GCBH searches generate thousands of configurations and may revisit structurally equivalent states multiple times, distinct surface structures were identified using an automated de-duplication procedure. Structures were first separated by stoichiometry and free energy and were subsequently compared using SOAP descriptors of their atomic environments, as described in the Supporting Information. Repeated or structurally equivalent configurations were grouped together before evaluating the Boltzmann populations shown in Figure 1e. Thus, each population in Figure 1e corresponds to a distinct atomistic surface structure rather than to a particular hydroxyl-coverage. Representative metastable structures contributing to these populations are shown in Figures S11-S13 of the Supporting Information. Note that the Boltzmann populations shown in Figure 1e are calculated only for the sampled configurations of each selected surface termination and are not averaged across all exposed facets using their Wulff area fractions. Thus, Figure 1e should be interpreted as a comparison of the configurational diversity of the modeled surface terminations under FCC-relevant steam conditions, rather than as a crystallite-area-weighted distribution of hydroxyl species. Nevertheless, to keep the discussion focused, we center the analysis below on the lowest-free-energy hydroxylated structure for each surface, since this motif remains the single largest contributor in most cases. The only exception is 2:1 mullite, for which two surfaces are equally stable. Therefore, both are considered to find the strongest Brønsted acid site (Figure S8).

Notably, the predicted hydroxyl coverage decreases with increasing vacancy content, which is counterintuitive if one assumes that less stable (more defective) surfaces should hydroxylate more extensively. Instead, we find that vacancy-rich compositions undergo significant reconstruction, in which the surface rearrangements partially compensate for the intrinsic vacancy-driven instability, thereby reducing the thermodynamic driving force for high hydroxyl coverages (Figure 1c).

In terms of local Al-coordination, sillimanite contains Al in equal proportions of tetrahedral (Al^{IV}) and octahedral (Al^{VI}) environments. As vacancies are introduced (moving toward more Al-rich mullites), part of the Al^{IV} and Al^{VI} population is converted into Al^{V} in bulk, consistent with local structural relaxation around vacancies. Slab formation perturbs the coordination distribution near the surface. Surface formation truncates some Al^{VI}, converting them into Al^{IV} and Al^{V} motifs thereby increasing the abundance of undercoordinated Al at the surface relative to the bulk (Figure 1d).

Remarkably, under FCC-relevant steam chemical potentials, most mullite phases develop zeolite-like bridging Brønsted acid sites (BAS) (Figure 1f), except 3.5:2 mullite. This indicates that zeolite-like bridging BAS formation is not limited to a single "ideal" composition but instead emerges whenever the reconstruction near the surface can generate direct Si-O-Al connectivity with an appropriately coordinated Al center. In contrast, 3.5:2 mullite remains dominated by terminal aluminols/silanols (and occasionally water-assisted motifs), reflecting a lack of the local Si-Al arrangements required to stabilize the bridging Brønsted acid site.

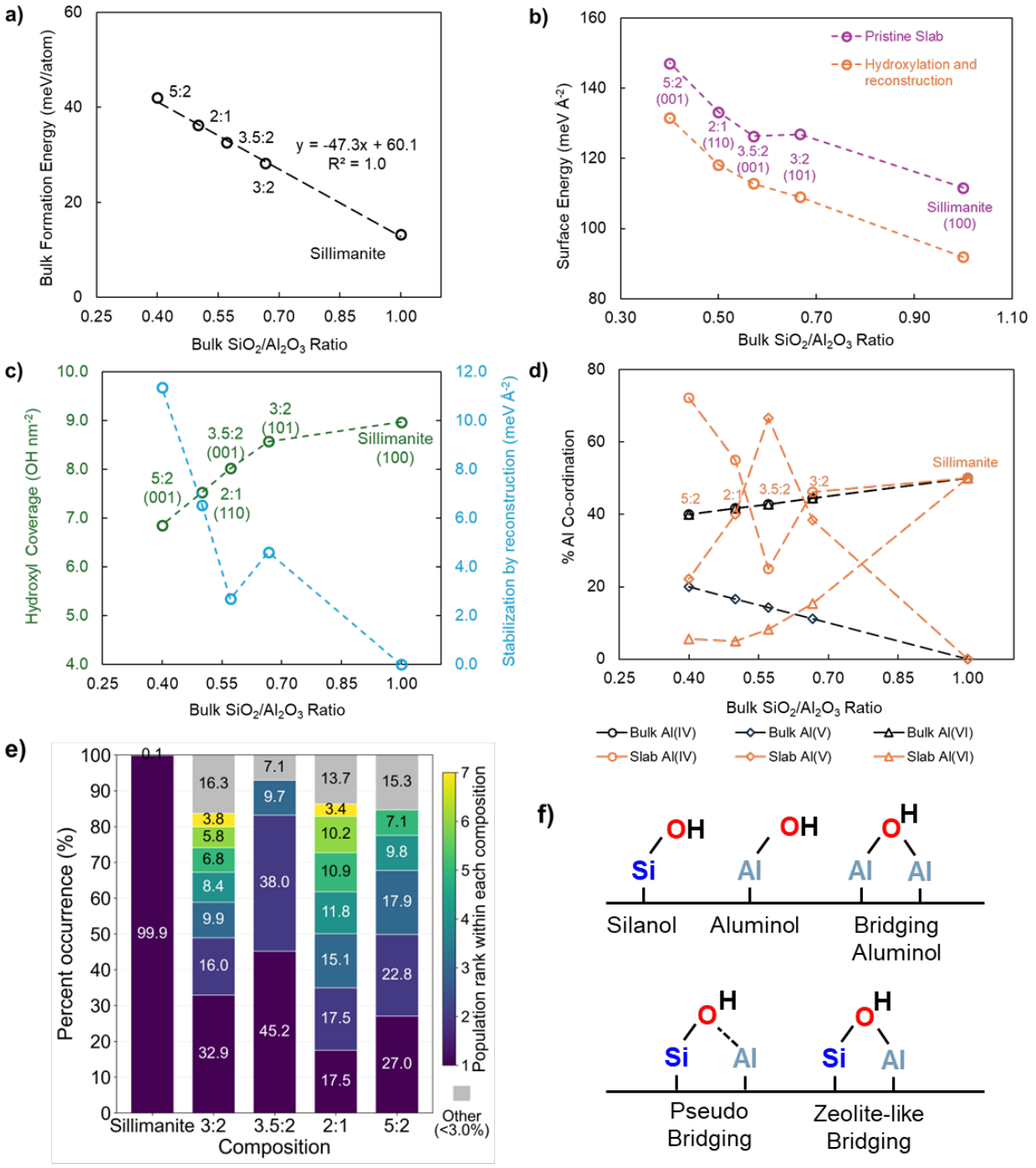

Figure 1: *(a) Bulk formation energies of mixed aluminosilicates as a function of the bulk SiO_2/Al_2O_3 ratio. Decreasing Si content increases the vacancy concentration and makes the formation energy less favorable (more positive) (b) Surface energies of the most stable facet for each stoichiometry; orange markers indicate hydroxylated, reconstructed structures obtained via grand-canonical basin hopping under FCC*

conditions (T = 550°C and P_{H_2O} = 1.2 bar). (c) Extent of hydroxylation and stabilization from reconstruction across mullite and sillimanite surfaces. At lower silica content, the high vacancy density shifts stabilization toward reconstruction rather than hydroxylation. (d) The fraction of Al atoms in tetra- (IV; circles), penta- (V; diamonds), and octa- (VI; triangles) coordination is shown for mullite as a function of stoichiometry, comparing the bulk (black lines) and slab models (orange lines). For slab models, the surface is defined as the top 25% of slab thickness. The cutoff for Al-O is 2.2 Å (e) Stacked bar chart showing the Boltzmann population distribution of surface structures at 550 °C and P_{H_2O} = 1.2 bar for sillimanite and mullite compositions. For each composition, the height of each colored segment represents the percent occurrence of a distinct surface structure within the ensemble, ordered by decreasing population rank. Population values are annotated for structures contributing more than 3.0%, and the remaining minor structures are grouped into the gray "Other (<3.0%)" category. Here, a distinct surface structure refers to a unique combination of surface stoichiometry and atomic arrangement. The energetics for (e) were determined using MLIP, while the energetics in (a)-(d) were determined using DFT. (f) Representative atomistic structures illustrating the different hydroxyl motifs present on aluminosilicate surfaces.

We quantified Brønsted acidity using the ammonia binding energy, (ΔE_{NH_3}) as an acidity descriptor to confirm the relevance of these sites for cracking reactions. Because NH_3 is a small probe molecule, its adsorption energy is used here primarily as a comparative descriptor of intrinsic Brønsted acidity rather than as a direct measure of cracking activity. To assess whether the strongest NH_3 binding sites are also accessible to a larger and experimentally relevant base, we performed additional DFT calculations for pyridine adsorption on selected strong Brønsted acid sites. Pyridine is widely used in FTIR experiments to distinguish Brønsted and Lewis acid sites in aluminosilicates [31], and its larger size provides a useful check against possible NH_3 specific confinement or H-bonding effects. The calculated pyridine adsorption energies, summarized in

Figure S10, follow the same qualitative trend as the NH_3 binding energies, indicating that the strongest NH_3-binding sites are also accessible to pyridine and are not artifacts of the small probe size.

Direct relevance to cracking reactivity, however, would require future calculations with hydrocarbon reactants or representative cracking intermediates. These surfaces can host a variety of BAS, including terminal and bridging hydroxyls as well as hydroxyl groups associated with adsorbed water, and their relative populations depend on the specific surface termination and degree of hydration (Figure 1f). The distribution of NH_3 adsorption energies further shows that the overall hydroxyl population is dominated by weakly to moderately acidic sites, consistent primarily with aluminol- and silanol-type species, whereas strongly binding sites are comparatively sparse (≈ 0.3 - 0.6 site nm^{-2} | Figure S4). Note that all reported hydroxyl, acid-site, and silica coverages are normalized by the exposed area of the modeled surface/facet. For polar slabs with chemically distinct top and bottom terminations, each termination was analyzed independently and normalized by the same single-face surface area. Therefore, reported values such as sites nm^{-2} or Si nm^{-2} are facet/termination-specific areal densities and are not averaged over the Wulff morphology unless explicitly stated. In the discussion below, we focus on the strongest NH_3 binding sites to characterize the upper range of intrinsic Brønsted acidity accessible on each modeled surface. These sites should not necessarily be interpreted as dominating the crystallite-scale acid-site population, which additionally depends on their areal density and on the abundance of the corresponding facet and surface termination. In our previous work on Si-doped γ-Al_2O_3 (spinel phase), we reported that isolated silanol and aluminol groups exhibited ΔE_{NH_3} values of -20 to -80 kJ mol^{-1}, comparable to pure alumina or silica. The bridging and pseudo-

bridging hydroxyls on Si/γ-Al_2O_3 were stronger, with ΔE_{NH_3}≈ -90 to -110 kJ mol^{-1} but far below the Brønsted acid sites in bulk MFI zeolites, where ΔE_{NH_3} ranges from -133 to -170 kJ mol^{-1}. In contrast, the Al-OH-Si bridging sites identified on 3:2 and 5:2 mullite exhibit markedly stronger Brønsted acidity than Si-doped γ-Al_2O_3, with ΔE_{NH_3} reaching -140 and -150 kJ mol^{-1}, respectively (Figure 2e,h). The values are more exothermic than those obtained for the spinel-derived bridging motifs and comparable to strong external zeolitic acid sites (ΔE_{NH_3}≈ -113 to -150 kJ mol^{-1}) [32]. By comparison, the Al-OH-Si bridging site on 2:1 mullite binds NH_3 weakly, showing ΔE_{NH_3}= -102 kJ mol^{-1}, more consistent with the acidity previously reported for Si-doped γ-Al_2O_3 (Figure 2c,g). This clear separation in acidity tracks directly with the local aluminum coordination at the bridging hydroxyl. The high acidity in 3:2 and 5:2 mullite originates from a bridging environment in which the BAS is associated with a tetrahedrally coordinated Al^{IV} center, which more effectively polarizes the O-H bond and stabilizes the conjugate base upon deprotonation, thereby strengthening NH_3 binding. In contrast, the bridging BAS in the spinel phase and in 2:1 mullite predominantly involve penta-coordinated Al^{V}. This coordination environment is less electron-withdrawing and provides greater local relaxation/screening, resulting in weaker Brønsted acidity and correspondingly weaker binding. Together, these trends demonstrate that not all "bridging-like" hydroxyls are equivalent. The presence of an Al-OH-Si linkage is necessary but not sufficient for high Brønsted acidity. The local Al coordination (Al^{IV} vs Al^{V}) is the key structural determinant controlling the strength of the BAS.

To distinguish intrinsic Brønsted acidity from possible confinement effects, we analyzed the local NH_3 adsorption geometries in Figure 2 by identifying the number of H-bonds to the protonated NH_4^+ species and the dispersion contribution to the binding energy. In the 2:1, 3:2, and 5:2 mullite cases, NH_3 is protonated to NH_4^+ and forms exactly three H-bonds with the surface in each

296 structure. Therefore, the number of H-bonds cannot be the origin of the stronger NH_3 binding in
297 3:2 and 5:2 mullite relative to 2:1 mullite. To separate dispersion from intrinsic acid strength, we
298 evaluated the dispersion component from the VASP dDsC dispersion correction for the adsorbed
299 slab, clean slab, and isolated NH_3. The dispersion contribution is attractive for all sites, ranging
300 from -14.5 to -31.8 kJ mol^{-1}, with the largest value for 3:2 mullite. However, dispersion does not
301 follow the total NH_3 binding trend. For example, 5:2 mullite shows the strongest NH_3 binding
302 energy, -150 kJ mol^{-1}, but only a moderate dispersion contribution of -19.3 kJ mol^{-1}. Thus,
303 dispersion and confinement provide secondary stabilizations, while the dominant origin of stronger
304 binding is the intrinsic Brønsted acidity of the local Al-O(H)-Si motif.
305 Consistent with the absence of true Al-OH-Si bridging motifs, 3.5:2 mullite does not show strong
306 acidic BAS. Instead, the strongest acidity arises when NH_3 binds to a hydroxyl associated with an
307 H_2O molecule adsorbed at an Al site, giving ΔE_{NH_3}= -99 kJ mol^{-1} (Figure 2f), which is stronger
308 than the values observed for non-bridging aluminol/silanol sites. Notably, 3.5:2 mullite also shows
309 the lowest population of tetrahedrally coordinated Al^{IV} among the mullite compositions studied
310 (Figure 1d). The scarcity of Al^{IV} environments is consistent with its inability to form zeolite-like
311 bridging BAS. In the next section, we investigate Si doping as a potential strategy to activate these
312 otherwise inactive surfaces.

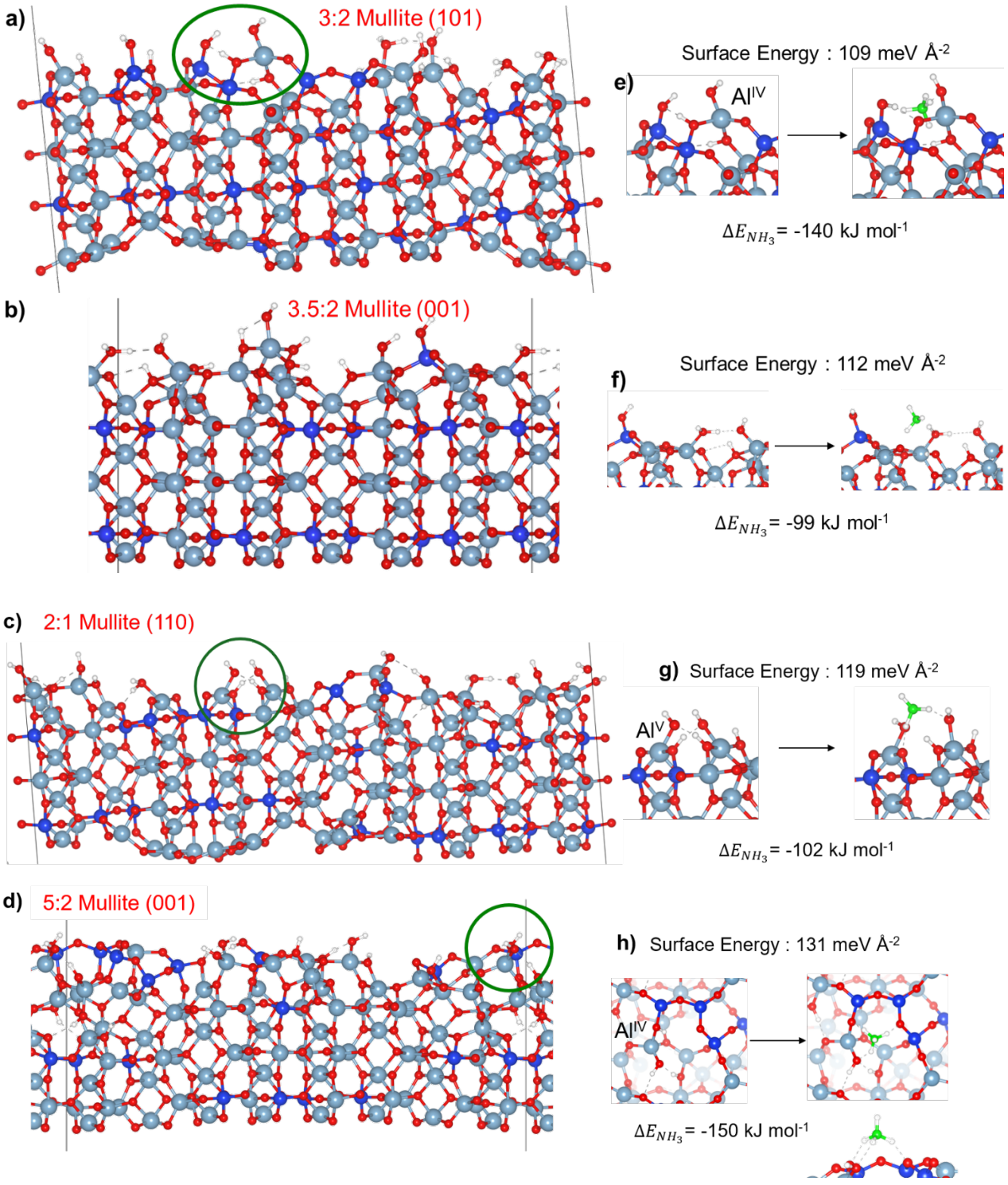

Figure 2: *Atomic structure of hydroxylated mullite under FCC conditions (T = 550°C and P_{H_2O} = 1.2 bar) using grand canonical basin hopping. Hydroxylated surface of the most stable termination for (a) 3:2 mullite, (b) 3.5:2 mullite, (c) 2:1 mullite and (d) 5:2 mullite. (e-h) NH_3 binding on the most acidic surface*

proton for (e) 3:2, (f) 3.5:2, (g) 2:1 mullite and (h) 5:2 mullite. White, green, light blue, dark blue, and red spheres represent H, N, Al, Si, and O, respectively. The solid black outline denotes the surface unit cell. Surface energies and NH_3 binding energies were computed using DFT. Green ellipse/circle outlines the zeolite-like bridging Brønsted acid site.

Silica Doped Mullite Surfaces under Reaction Conditions

The weak acidity of 3.5:2 mullite can potentially be similar to that seen in the extensive literature on γ-Al_2O_3, where silica addition is essential to generate Brønsted acidity with Si-doped γ-Al_2O_3 (spinel phase)[10,20,33]. In the *in situ* synthesis route for FCC matrix, during calcination kaolin is first dehydrated to metakaolin, which subsequently reorganizes into a biphasic mixture of γ-Al_2O_3 and amorphous SiO_2[30], forming the Si-doped/stabilized spinel intermediate[12]. Upon further thermal treatment, this intermediate transforms into mullite[34]. This transformation proceeds via a shift in Al_2O_3/SiO_2 ratio toward the thermodynamic stoichiometry of mullite (e.g., 2:1 or 3:2 Al_2O_3:SiO_2). BASF experiments on both as prepared and aged catalysts indicate coexistence of spinel and mullite domains[6,15]. Therefore, free or weakly bound silica is available at the surface exactly as spinel (Si-doped γ-Al_2O_3) domains crystallize into mullite. This silica can react with under-coordinated surface environments and seed interfacial aluminosilicate layers that stabilize acid-functional motifs, effectively reintroducing acidity on otherwise inert mullite surfaces. This compositional evolution can be summarized by a reaction network for silica release and uptake, illustrated by the progression from kaolinite ($Al_2O_3 \cdot 2SiO_2 \cdot 2H_2O$) to spinel (γ-$Al_2O_3$), and ultimately to 3:2 mullite, which is the most stable mullite stoichiometry[30] (Equations 1-4).

$$35\ (Al_2O_3 \cdot 2\ SiO_2 \cdot 2\ H_2O) \rightarrow 35\ \gamma\text{-}Al_2O_3 + 70\ SiO_2 + 70\ H_2O \qquad \text{Eq.1}$$

$$35\ \gamma\text{-}Al_2O_3 + 70\ SiO_2 \rightarrow 7(5\ Al_2O_3{:}2\ SiO_2) + 56\ SiO_2 \qquad \text{Eq.2}$$

$$7(5\ Al_2O_3{:}2\ SiO_2) + 56\ SiO_2 \rightarrow 10\ (3.5\ Al_2O_3{:}2\ SiO_2) + 50\ SiO_2 \qquad \text{Eq.3}$$

$$10\ (3.5\ Al_2O_3{:}2\ SiO_2) + 50\ SiO_2 \rightarrow 35/3\ (3\ Al_2O_3{:}2\ SiO_2) + 140/3\ SiO_2 \qquad \text{Eq.4}$$

Building on our earlier work, where we exhaustively enumerated Si-doped and hydroxylated configurations, we employ a more flexible sampling strategy here. Silica was systematically deposited onto multiple mullite surface terminations, and for each SiO_2 coverage we performed grand-canonical basin hopping (GCBH) while allowing water adsorption/desorption at fixed chemical potential of water. For the thermodynamically preferred (001) termination of 3.5:2 mullite, we scanned SiO_2 coverages from 0.0 to 3.4 Si nm^{-2} corresponding to 0-6 SiO_2 units per surface unit cell. Because this (001) slab is polar, with non-equivalent top and bottom terminations, we explicitly examined silica addition on both surfaces (top (a) - and bottom (b) -terminated) to capture termination-specific stabilization and avoid bias from choosing a single termination. For 5:2 mullite, we varied the coverage from 0.0 to 1.3 Si nm^{-2} (0-3 SiO_2 units per surface unit cell). We focused on these stoichiometries primarily for computational tractability. The 2:1 and 3:2 mullite surfaces require substantially larger surface unit cells, making equivalent coverage sweeps and GCBH sampling unfeasible.

We find that deposited silica preferentially binds at surface vacancies and defects that, on pristine mullite can promote dissociative water adsorption. As the silica loading increases, the near-surface region progressively reconstructs into a more disordered, amorphous-like interface, with Si migrating from subsurface regions to the surface, and in some cases vice versa (Figures S4–S6). The surface energy associated with silica incorporation varies only weakly with coverage, and several coverages are slightly stabilized when referenced to bulk SiO_2 (Figure 3a). Additionally, the relative stability ordering of 5:2 versus 3.5:2 does not change upon silica addition, hydroxylation, or the accompanying reconstruction. For 3.5:2 mullite, the equilibrium hydroxyl coverage decreases with increasing silica loading (Figure 3b), consistent with progressive

passivation of hydroxylation-active sites and/or replacement of hydroxyls by Si-O-Si linkages. In contrast, the hydroxyl coverage on 5:2 mullite remains approximately constant with silica addition, suggesting that hydroxylation is instead controlled by the high density of persistent vacancy-derived adsorption sites that are not fully quenched over the silica coverages explored.

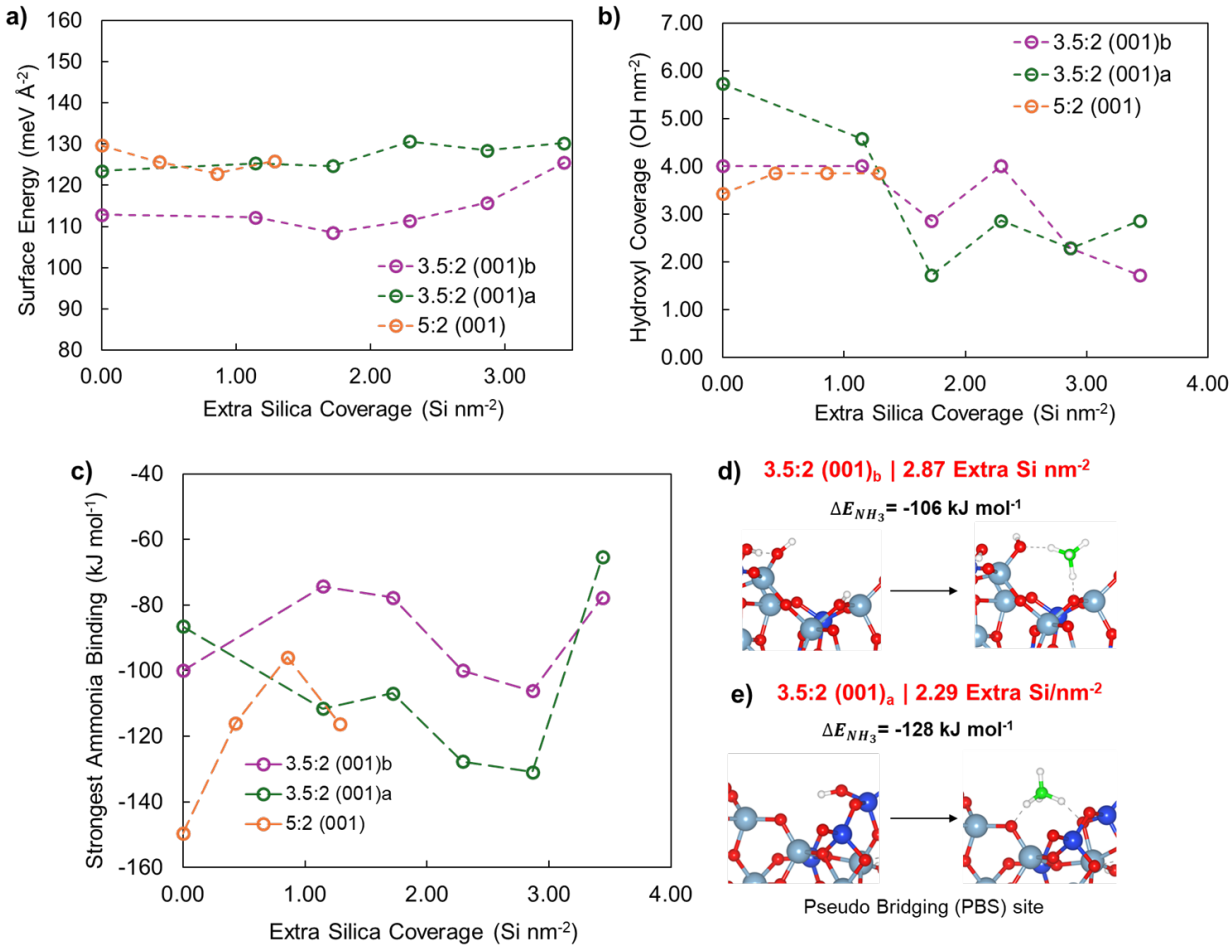

Figure 3: *(a) Surface energies of the Si-doped 3.5:2 and 5:2 mullites via grand-canonical basin hopping under FCC conditions (T = 550°C and P_{H_2O} = 1.2 bar). (b) Extent of hydroxylation plotted as a function of increasing SiO_2 doping. (c) Strongest ammonia binding ΔE_{NH_3} for three different mullite surfaces plotted as a function of increasing SiO_2 doping. (d) Side view of NH_3 binding on Si-doped 3.5:2 $(001)_b$ mullite surface. (e) Side view of NH_3 binding on Si-doped 3.5:2 $(001)_a$ mullite surface. The pseudo-bridging silanol site is depicted in (e). The light blue, dark blue, red, white, and green colors represent Al, Si, O, H and N*

atoms respectively. The dotted black line represents H-bonds. Side and top view of the entire unit cell are depicted in Figure S5-S7

As in the previous section, we use ammonia binding energy (ΔE_{NH_3}) as an acidity descriptor to quantify Brønsted acidity. For 3.5:2 mullite, the strongest NH_3 binding exhibits a dependence on silica loading, passing through a minimum (stronger acidity) at an intermediate coverage (Figure 3c), similar to trends reported for Si-doped γ-Al_2O_3 (spinel) [22]. On the less stable $(001)_a$ termination, this minimum corresponds to a pseudo-bridging site (PBS), where NH_3 binds to a silanol located adjacent to an undercoordinated Al center, and proton transfer stabilizes a conjugate base with significant charge localization (Figure 3e). In contrast, on the more stable $(001)_b$ termination, the minimum initially coincides with the formation of a zeolite-like bridging BAS. However, at the optimal coverage, we identify a new Brønsted acid motif in which NH_3 binds to bridging aluminol, with Al^{IV}-O-Al^{IV} connectivity, while also forming hydrogen bonds with neighboring aluminol (Figure 3d). Together, these results reinforce our earlier conclusion that aluminosilicate surfaces can host a diverse ensemble of strong acid motifs whose prevalence depends sensitively on local composition and reconstruction. As silica is added to 3.5:2 mullite, the fraction of surface Al^{IV} sites increases and passes through a maximum at intermediate coverage (Figure S9), mirroring the nonmonotonic dependence of NH_3 binding strength on silica loading shown in Figure 3c. This correlation suggests that silica addition promotes the formation of low coordinate Al environments associated with stronger Brønsted acidity.

By contrast, for 5:2 mullite, silica addition suppresses the strongest Brønsted sites. Silica preferentially passivates reactive Al^{IV} environments through Si-O linkages, reducing the availability of reactive hydroxyl motifs. Accordingly, the most favorable NH_3 binding becomes progressively weaker with increasing silica loading. Additionally, increasing silica coverage

reduces the fraction of tetrahedrally coordinated Al^{IV} sites (Figure S9), while the fractions of penta- and octa-coordinated Al increase. Thus, the weakening of NH_3 binding with silica addition is accompanied by a loss of Al^{IV} motifs, indicating that the strongest acidity on 5:2 mullite is closely associated with these low-coordinate surface environments.

The opposite responses of 3.5:2 and 5:2 mullite can be rationalized by their different intrinsic near-surface Si distributions prior to silica doping (Figure 4a). Although 5:2 mullite is Si-poor in the bulk, its vacancy-rich framework promotes the segregation of a larger fraction of the available Si to the reconstructed near-surface region, reaching approximately 3.0 Si nm^{-2}. This enrichment, together with the reduced tendency to form bulk Si-Si pairs, facilitates near-surface Si-Al linkages that can generate very strong bridging Brønsted acid motifs in the undoped material. In contrast, 3.5:2 mullite contains enough bulk Si to favor greater Si-Si connectivity, leaving fewer isolated Si centers near the surface and therefore fewer possibilities to form strong Al-O(H)-Si motifs without additional silica. Silica therefore activates 3.5:2 by supplying surface accessible Si to generate bridging/pseudo-bridging motifs, whereas it quenches 5:2 by saturating the Al^{IV} rich environments responsible for high acidity. Overall, these results highlight that surface Si concentration depends nonlinearly on bulk composition and reconstruction, and that the impact of added silica depends on the pre-existing defects and Si distribution landscape.

411

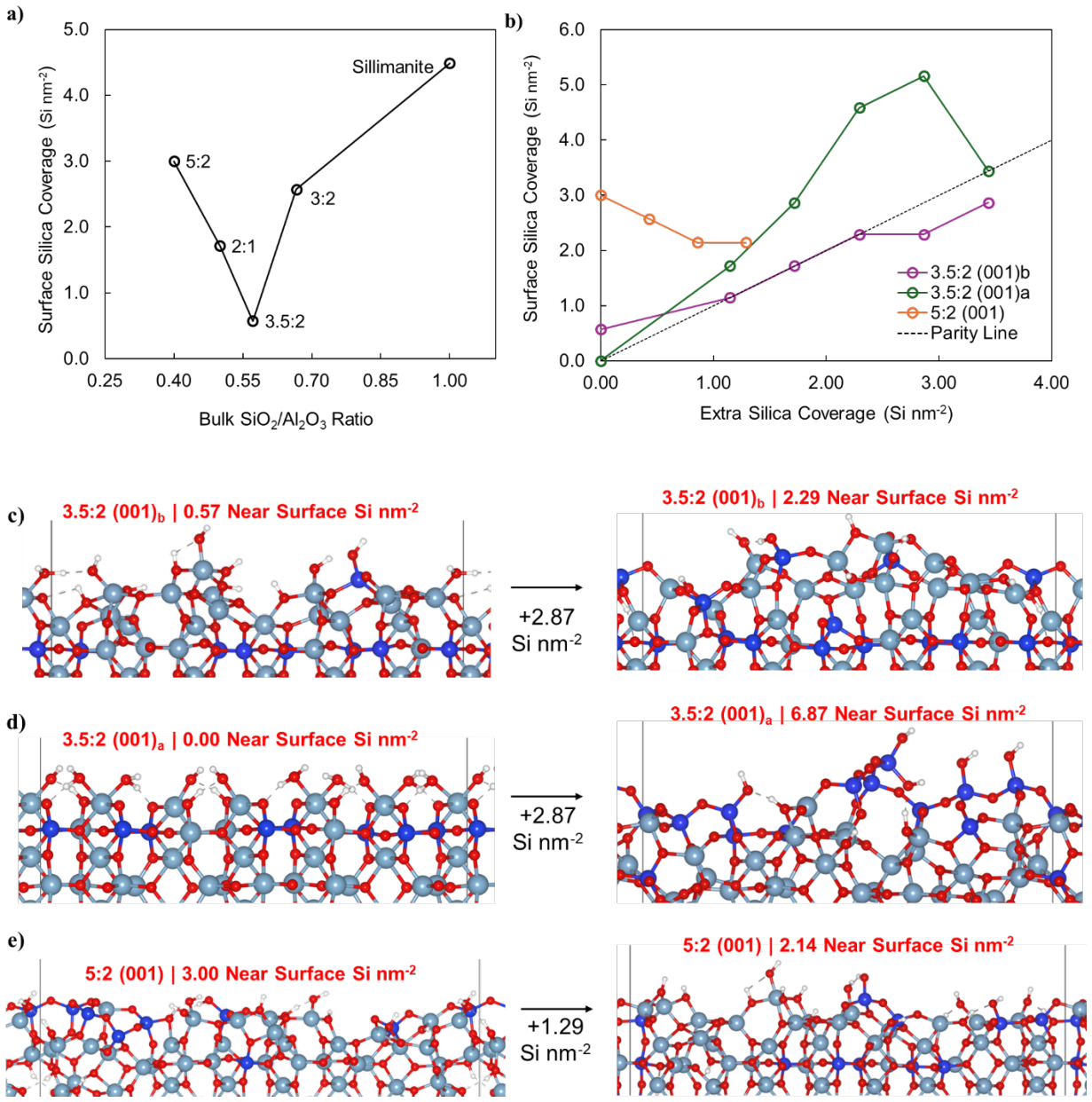

412

413 ***Figure 4:*** *(a) Near-surface silica coverage for the most stable mullite surfaces and sillimanite. (b) Near-*
414 *surface silica coverage for the most stable mullite surfaces after silica doping, shown as a function of*
415 *increasing SiO_2 loading. The deposited silica may remain at the surface or migrate into the subsurface.*
416 *Structural evolution upon SiO_2 deposition followed by grand-canonical basin hopping under FCC*
417 *conditions (T = 550 °C, P_{H_2O} = 1.2 bar) is shown for (c) 3.5:2 mullite $(001)_b$, (d) 3.5:2 mullite $(001)_a$, and*
418 *(e) 5:2 mullite (001).*

Conclusions

In this study, we establish an atomistic picture of how Brønsted acidity emerges (or disappears) on mullite surfaces under FCC-relevant conditions by combining DFT, MLIP-accelerated relaxation, and grand-canonical basin hopping sampling. Additionally, by using NH_3 binding energy as an acidity probe, chosen for its robustness in periodic calculations and its compatibility with MLIP workflows, we connect realistic hydroxylated/reconstructed surface ensembles directly to its Brønsted acid strength.

We observe that mullite surfaces can host acid sites of a strength similar to that of external zeolitic acid sites. Further, we show that Brønsted acidity is controlled by local coordination chemistry and not by "bridging-like" geometry alone. The strongest Brønsted acid sites in 3:2 and 5:2 mullite arise when the bridging Brønsted acid site is associated with a tetrahedrally coordinated Al^{IV} environment. In contrast, NH_3 binding on bridging-like motifs involving Al^{V} (common in spinel-like environments and in 2:1 mullite) is much weaker. More broadly, comparison with the calculated Wulff morphologies emphasizes that the catalytic relevance of such motifs depends on both their intrinsic acid strength and the abundance of the facet on which they occur.

We further demonstrate that silica redistribution during kaolin → spinel → mullite evolution can act as an "activator" of otherwise weakly acidic mullite terminations. The formation of surface acidic Si-OH-Al units shows a complex non-linear dependence on the bulk Si content of the mullite phase. For the intrinsically weakly acidic 3.5:2 mullite, surface silica grafting generates a coverage-dependent acidity that passes through an optimum, producing a diverse ensemble of strong acid motifs, including zeolite-like bridging and pseudo-bridging BAS. In contrast, silica addition can passivate the strongest sites on highly vacancy-rich surfaces (5:2 mullite) by quenching reactive Al^{IV} environments, highlighting that the impact of silica is non-universal and

depends on the vacancy/defect landscape, the number of Si atoms present at the undoped mullite surface and reconstruction pathways. Silica addition can either generate strong motifs on otherwise inactive surfaces or quench the coordination environments required for ultrahigh acidity.

In conclusion, this work advances the understanding of FCC-relevant aluminosilicates by providing atomistic insight into the structural factors that govern Brønsted acid site formation on mullite surfaces. By identifying Al^{IV} coordination and coverage-dependent silica restructuring as key descriptors, our results offer guidance for catalyst design. Specifically, they suggest that matrix acidity can be tuned through controlled silica availability and defect management, with implications for improving performance in industrial catalytic cracking processes.

AUTHOR INFORMATION

Corresponding Authors

*Philippe Sautet − Chemical and Biomolecular Engineering Department, University of California Los Angeles, California, United States; Email: sautet@ucla.edu

Author Contributions

K. J. S. performed the electronic structure calculations under the guidance of D.S., A.D., L.D., R.S.C. and P.S. The manuscript was written through contributions of all authors. All authors have given approval to the final version of the manuscript.

Notes: D.S., A.D., L.D., and R.S.C. are employees of BASF Corporation. This work was financially supported by the California Research Alliance by BASF. The remaining authors declare no competing financial interest.

ASSOCIATED CONTENT

The Supporting Information contains the full computational workflow used in this study, including DFT settings [22,35–38], bulk and slab model construction for sillimanite and multiple mullite stoichiometries[22,23], development and validation of the NequIP[27] based machine learning potentials, the grand-canonical basin hopping sampling protocol[29], and the ammonia-binding calculations used to quantify Brønsted acidity[32]. It also includes supplementary tables and figures presenting bulk mullite and sillimanite structures, surface energetics, MLIP parity plots, NH_3 adsorption-energy distributions, and representative surface models for Si-doped mullite surfaces. Additional references relevant to the computational methods and supporting analyses are cited in the Supporting Information.

ACKNOWLEDGMENT

The authors acknowledge financial support from the California Research Alliance by BASF (CARA). K.J.S. and P.S. acknowledge computational support from UCLA Advanced Research Computing. This work used Bridges2 cluster at Pittsburgh Supercomputing Center through allocation CHM240032 from the Advanced Cyberinfrastructure Coordination Ecosystem: Services & Support (ACCESS) program, which is supported by U.S. National Science Foundation grants #2138259, #2138286, #2138307, #2137603, and #2138296.

OpenAI's ChatGPT was used during manuscript preparation and revision to assist with language editing, grammar, clarity, and organization, and to review the manuscript for consistency and formatting. The authors reviewed and edited all AI-assisted text and take full responsibility for the content of the manuscript.

References

(1) Plank, C. J.; Rosinski, E. J.; Hawthorne, W. P. Acidic Crystalline Aluminosilicates. New Superactive, Superselective Cracking Catalysts. *I&EC Product Research and Development* **1964**, *3* (3), 165–169. https://doi.org/10.1021/i360011a001.

(2) Busca, G. Acid Catalysts in Industrial Hydrocarbon Chemistry. *Chem. Rev.* **2007**, *107* (11), 5366–5410. https://doi.org/10.1021/cr068042e.

(3) Biswas, J.; Maxwell, I. E. Recent Process- and Catalyst-Related Developments in Fluid Catalytic Cracking. *Appl. Catal.* **1990**, *63* (1), 197–258. https://doi.org/10.1016/S0166-9834(00)81716-9.

(4) Vogt, E. T. C.; Weckhuysen, B. M. Fluid Catalytic Cracking: Recent Developments on the Grand Old Lady of Zeolite Catalysis. *Chem. Soc. Rev.* **2015**, *44* (20), 7342–7370. https://doi.org/10.1039/C5CS00376H.

(5) Goldsmith, B. R.; Peters, B.; Johnson, J. K.; Gates, B. C.; Scott, S. L. Beyond Ordered Materials: Understanding Catalytic Sites on Amorphous Solids. *ACS Catal.* **2017**, *7* (11), 7543–7557. https://doi.org/10.1021/acscatal.7b01767.

(6) Gibson, C. W.; Willis, M. J.; Gantt, G. E.; Barnes, R. E.; Stockwell, D. M. Fcc Catalyst Manufacturing Process, 2004. https://patents.google.com/patent/EP1420883A1/en.

(7) Murrell, L. L.; Nicholas C. Dispenziere, Jr. Catalysts Comprising Silica Supported on a Boehmite-like Surface, Their Preparation and Use, November 1987. https://patents.google.com/patent/US4708945A/en.

(8) Folmar, K.; Willis, M. Thermochemical Structuring of Matrix Components for FCC Catalysts. US13042808, January 27, 2015. https://patents.google.com/patent/US8940156B2/en (accessed 2025-08-19).

(9) Liu, Y.; Pinnavaia, T. J. Aluminosilicate Nanoparticles for Catalytic Hydrocarbon Cracking. *J. Am. Chem. Soc.* **2003**, *125* (9), 2376–2377. https://doi.org/10.1021/ja029336u.

(10) Caillot, M.; Chaumonnot, A.; Digne, M.; Bokhoven, J. A. V. Quantification of Brønsted Acid Sites of Grafted Amorphous Silica-Alumina Compounds and Their Turnover Frequency in m-Xylene Isomerization. *ChemCatChem* **2013**, *5* (12), 3644–3656. https://doi.org/10.1002/cctc.201300560.

(11) Hensen, E. J. M.; Poduval, D. G.; Degirmenci, V.; Ligthart, D. A. J. M.; Chen, W.; Maugé, F.; Rigutto, M. S.; Veen, J. A. R. Van. Acidity Characterization of Amorphous Silica-Alumina. *Journal of Physical Chemistry C* **2012**, *116* (40), 21416–21429. https://doi.org/10.1021/jp309182f.

(12) Okada, K.; ŌTsuka, N.; Ossaka, J. Characterization of Spinel Phase Formed in the Kaolin-Mullite Thermal Sequence. *Journal of the American Ceramic Society* **1986**, *69* (10). https://doi.org/10.1111/j.1151-2916.1986.tb07353.x.

(13) Fischer, R. X.; Schneider, H.; Rahman, S.; Freimann, S. Crystal Chemistry of Mullite and Related Phases: Sections 1.1 - 1.2. In *Mullite*; Wiley, 2005; pp 1–70. https://doi.org/10.1002/3527607358.ch1a.

(14) Kovářík, T.; Bělský, P.; Novotný, P.; Říha, J.; Savková, J.; Medlín, R.; Rieger, D.; Holba, P. Structural and Physical Changes of Re-Calcined Metakaolin Regarding Its Reactivity. *Constr. Build. Mater.* **2015**, *80*, 98–104. https://doi.org/10.1016/j.conbuildmat.2014.12.062.

(15) Stockwell, D. M.; Liu, X.; Nagel, P.; Nelson, P. J.; Gegan, T. A.; Keweshan, C. F. Distributed Matrix Structures—Novel Technology for High Performance in Short Contact Time FCC. *Stud. Surf. Sci. Catal.* **2004**, *149*, 257–285. https://doi.org/10.1016/s0167-2991(04)80768-7.

(16) Caillot, M.; Chaumonnot, A.; Digne, M.; Van Bokhoven, J. A. The Variety of Brønsted Acid Sites in Amorphous Aluminosilicates and Zeolites. *J. Catal.* **2014**, *316*, 47–56. https://doi.org/10.1016/j.jcat.2014.05.002.

(17) Valla, M.; Rossini, A. J.; Caillot, M.; Chizallet, C.; Raybaud, P.; Digne, M.; Chaumonnot, A.; Lesage, A.; Emsley, L.; Van Bokhoven, J. A.; Copéret, C. Atomic Description of the Interface between Silica and Alumina in Aluminosilicates through Dynamic Nuclear Polarization Surface-Enhanced NMR Spectroscopy and First-Principles Calculations. *J. Am. Chem. Soc.* **2015**, *137* (33), 10710–10719. https://doi.org/10.1021/jacs.5b06134.

(18) Chizallet, C.; Raybaud, P. Pseudo-Bridging Silanols as Versatile Brønsted Acid Sites of Amorphous Aluminosilicate Surfaces. *Angew. Chem. Int. Ed.* **2009**, *48* (16), 2891–2893. https://doi.org/10.1002/anie.200804580.

(19) Leydier, F.; Chizallet, C.; Costa, D.; Raybaud, P. Revisiting Carbenium Chemistry on Amorphous Silica-Alumina: Unraveling Their Milder Acidity as Compared to Zeolites. *J. Catal.* **2015**, *325*, 35–47. https://doi.org/10.1016/j.jcat.2015.02.012.

(20) Poduval, D. G.; Van Veen, J. A. R.; Rigutto, M. S.; Hensen, E. J. M. Brønsted Acid Sites of Zeolitic Strength in Amorphous Silica-Alumina. *Chemical Communications* **2010**, *46* (20), 3466–3468. https://doi.org/10.1039/c000019a.

(21) Hensen, E. J. M.; Poduval, D. G.; Magusin, P. C. M. M.; Coumans, A. E.; Veen, J. A. R. van. Formation of Acid Sites in Amorphous Silica-Alumina. *J. Catal.* **2010**, *269* (1), 201–218. https://doi.org/10.1016/j.jcat.2009.11.008.

(22) Sawant, K. J.; Stockwell, D.; Debellis, A.; Dorazio, L.; Sautet, P. Ensemble of Active Acid Sites on Amorphous Silica–Alumina Surfaces for Catalytic Cracking. *Angew. Chem. Int. Ed.* **2025**. https://doi.org/10.1002/anie.202506711.

(23) Klar, P. B.; Etxebarria, I.; Madariaga, G. Exploiting Superspace to Clarify Vacancy and Al/Si Ordering in Mullite. *IUCrJ* **2018**, *5* (4), 497–509. https://doi.org/10.1107/S2052252518007467.

(24) Birkenstock, J.; Petříček, V.; Pedersen, B.; Schneider, H.; Fischer, R. X. The Modulated Average Structure of Mullite. *Acta Crystallogr. B Struct. Sci. Cryst. Eng. Mater.* **2015**, *71* (3), 358–368. https://doi.org/10.1107/S205252061500757X.

(25) Klar, P. B.; Etxebarria, I.; Madariaga, G. Characterizing Modulated Structures with First-Principles Calculations: A Unified Superspace Scheme of Ordering in Mullite. *Acta Crystallogr. A Found. Adv.* **2019**, *75* (2), 260–272. https://doi.org/10.1107/S2053273319000846.

(26) Kluf, F. J.; Prochazka, S.; Doremus, R. H. Alumina-Silica Phase Diagram in the Mullite Region. *Journal of the American Ceramic Society* **1987**, *70* (10), 750–759. https://doi.org/10.1111/j.1151-2916.1987.tb04875.x.

(27) Batzner, S.; Musaelian, A.; Sun, L.; Geiger, M.; Mailoa, J. P.; Kornbluth, M.; Molinari, N.; Smidt, T. E.; Kozinsky, B. E(3)-Equivariant Graph Neural Networks for Data-Efficient and Accurate Interatomic Potentials. *Nat. Commun.* **2022**, *13* (1), 2453. https://doi.org/10.1038/s41467-022-29939-5.

(28) Wales, D. J.; Doye, J. P. K. Global Optimization by Basin-Hopping and the Lowest Energy Structures of Lennard-Jones Clusters Containing up to 110 Atoms. *J. Phys. Chem. A* **1997**, *101* (28), 5111–5116. https://doi.org/10.1021/jp970984n.

(29) Sawant, K. J.; Sautet, P. Modular Global Optimization Using Molecular Graphs : A Case Study of ZnO/Cu Surface for Methanol Synthesis Reaction. June 6, 2025. https://doi.org/10.26434/chemrxiv-2025-t71bx.

(30) Sonuparlak, B.; Sarikaya, M.; Aksay, I. A. Spinel Phase Formation During the 980°C Exothermic Reaction in the Kaolinite-to-Mullite Reaction Series. *Journal of the American Ceramic Society* **1987**, *70* (11), 837–842. https://doi.org/10.1111/j.1151-2916.1987.tb05637.x.

(31) Barzetti, T.; Selli, E.; Moscotti, D.; Forni, L. Pyridine and Ammonia as Probes for FTIR Analysis of Solid Acid Catalysts. *Journal of the Chemical Society, Faraday Transactions* **1996**, *92* (8), 1401. https://doi.org/10.1039/ft9969201401.

(32) Balcom, H.; Hoffman, A. J.; Locht, H.; Hibbitts, D. Brønsted Acid Strength Does Not Change for Bulk and External Sites of MFI Except for Al Substitution Where Silanol Groups Form. *ACS Catal.* **2023**, *13* (7), 4470–4487. https://doi.org/10.1021/acscatal.3c00076.

(33) Trombetta, M.; Busca, G.; Rossini, S.; Piccoli, V.; Cornaro, U.; Guercio, A.; Catani, R.; Willey, R. J. *FT-IR Studies on Light Olefin Skeletal Isomerization Catalysis III. Surface Acidity and Activity of Amorphous and Crystalline Catalysts Belonging to the SiO 2-Al 2 O 3 System*; 1998; Vol. 179.

(34) Martinón-Torres, M.; Rehren, T.; Freestone, I. C. Mullite and the Mystery of Hessian Wares. *Nature* **2006**, *444* (7118), 437–438. https://doi.org/10.1038/444437a.

(35) Kresse, G.; Furthmüller, J. Efficient Iterative Schemes for *Ab Initio* Total-Energy Calculations Using a Plane-Wave Basis Set. *Phys. Rev. B* **1996**, *54* (16), 11169–11186. https://doi.org/10.1103/PhysRevB.54.11169.

(36) Kresse, G.; Furthmüller, J. Efficiency of Ab-Initio Total Energy Calculations for Metals and Semiconductors Using a Plane-Wave Basis Set. *Comput. Mater. Sci.* **1996**, *6* (1), 15–50. https://doi.org/10.1016/0927-0256(96)00008-0.

(37) Pigeon, T.; Chizallet, C.; Raybaud, P. Revisiting γ-Alumina Surface Models through the Topotactic Transformation of Boehmite Surfaces. *J. Catal.* **2022**, *405*, 140–151. https://doi.org/10.1016/j.jcat.2021.11.011.

(38) Perdew, J. P.; Burke, K.; Ernzerhof, M. Generalized Gradient Approximation Made Simple. *Phys. Rev. Lett.* **1996**, *77* (18), 3865–3868. https://doi.org/10.1103/PhysRevLett.77.3865.

TOC